Journal of
Marine Science and Engineering

MDPI

Article

Effect of Wavelength on Turbine Performances and Vortical Wake Flows for Various Submersion Depths

Bohan Liu [1] and Sunho Park [1,2,*]

[1] Department of Convergence Studies on the Ocean Science and Technology, Korea Maritime and Ocean University, Busan 49112, Republic of Korea; liubohan@g.kmou.ac.kr
[2] Department of Ocean Engineering, Korea Maritime and Ocean University, Busan 49112, Republic of Korea
* Correspondence: spark@kmou.ac.kr

Abstract: When tidal turbines are deployed in water areas with significant waves, assessing the surface wave effects becomes imperative. Understanding the dynamic impact of wave–current conditions on the fluid dynamic performance of tidal turbines is crucial. This paper aims to establish a fundamental understanding of the influence of surface waves on tidal turbines. OpenFOAM, an open-source computational fluid dynamics (CFD) library platform, is utilized to predict the performance of current turbine under waves and currents. This research investigates the effects of two critical wave parameters, wave height and wavelength, on the fluid dynamics and wake structures of current turbine. Additionally, this study explores the influence of various submersion depths on turbine performance. The findings indicate that, under various wave conditions, the turbine's average power coefficient remains constant, but significant fluctuations are shown. Increasing submersion depth can mitigate the impact of waves. However, in regions characterized by longer wavelengths, altering the submersion depth has limited effects on turbine performance.

Keywords: computational fluid dynamics (CFD); current turbine; wave height and length; wave and current interaction

check for updates

Citation: Liu, B.; Park, S. Effect of Wavelength on Turbine Performances and Vortical Wake Flows for Various Submersion Depths. *J. Mar. Sci. Eng.* **2024**, *12*, 560. https://doi.org/10.3390/jmse12040560

Academic Editor: Eugen Rusu

Received: 26 February 2024
Revised: 14 March 2024
Accepted: 25 March 2024
Published: 27 March 2024

Copyright: © 2024 by the authors. Licensee MDPI, Basel, Switzerland. This article is an open access article distributed under the terms and conditions of the Creative Commons Attribution (CC BY) license (https://creativecommons.org/licenses/by/4.0/).

1. Introduction

In recent years, due to the escalating energy crisis, there has been a notable surge in the interest surrounding eco-friendly energy solutions. This has led to rapid advancements in the global development of ocean tidal energy [1]. Ocean current turbines serve as pivotal devices aimed at harnessing the energy from ocean currents to generate electricity. As ocean tides ebb and flow, the turbine blades rotate, which drives the turbine, subsequently generating electricity via an attached generator [2]. These turbines are commonly categorized into two types based on the angle between the rotation axis and the direction of the current flow [3]: vertical-axis tidal stream turbine (VATST) and horizontal-axis tidal stream turbine (HATST). Comparative studies have indicated that HATST exhibits a higher power coefficient and demonstrates fewer fluctuations in performance when compared to VATST [4]. Despite being influenced by the direction of incoming flow, HATST remains widely adopted due to its superior power efficiency [5,6].

The hydrodynamic performance of ocean current turbines plays a pivotal role in determining the overall power efficiency of these devices. Extensive research has been conducted to evaluate the hydrodynamic performance of horizontal-axis tidal stream turbines (HATST), encompassing investigations into various parameters such as blade numbers [7], floating structures [8], and turbulence intensity [9]. However, a common assumption in many studies is uniform and wave-free flow upstream. Contrary to this assumption, Lust et al. [10] have revealed that waves have minimal effect on the average performance of the turbine, and that they induce significant variations in thrust, rotation speed, and torque as they pass through. Gaurier et al. [11] have utilized a scaled model of a three-blade HATST with a rotor diameter of 0.9 m to investigate the influence of wave and current

interactions on measured strains. Their findings have underscored that solely considering the current load is inadequate for blade design, as fatigue performance is predominantly influenced by wave forces. Hence, acquiring a comprehensive understanding of both wave and current conditions is imperative for effective design. In a study by Galloway et al. [12], experiments were conducted by employing a 1:20 scale model of a three-blade HATST within a large towing tank. Their research revealed that for turbines operating in dynamic flow conditions, the out-of-plane bending moment significantly surpassed the in-plane bending moment, reaching 9.5 times its magnitude. Moreover, in contrast to wave-induced loads, the stable yawing load acting on an individual blade was deemed negligible. These insights shed light on the complex dynamics involved in tidal stream turbine operation and highlight the importance of considering various environmental factors for accurate design and performance assessments. Guo et al. [13] have further examined the hydrodynamic performance of turbines under waves using scaled models in towing tanks, discovering temporal fluctuations in torque and thrust, with oscillations reaching up to 50% of the mean values. Draycott et al. [14] have explored the hydrodynamic performance of scaled models under regular waves, finding that fluctuations induced by waves decrease with increasing wave frequency and increase with increasing wave amplitude. Additionally, hub submersion depth also significantly influences turbine performance. Zang et al. [15] have performed experiments on a tidal turbine model characterized by a diameter equivalent to 0.49 times the water depth. Their objective was to investigate how moderate waves affect the average wake characteristics and overall wake features of the turbine. Their study revealed notable findings regarding the interplay between waves and turbine wakes. Specifically, their research demonstrated that the turbulence intensity in the upper region of the wake is notably affected by wave height. Additionally, the study indicated that the wave period exerts a more substantial influence on the integral time scale compared to the impact of wave height, particularly in the far wake region. These insights provide valuable understanding into the complex interaction between tidal turbines and waves, offering implications for turbine design and performance optimization in real-world conditions. Kolekar and Banerjee [16] have determined that optimal turbine performance is achieved when the swept area of the turbine is positioned at least $0.25D$ below the surface and $0.5D$ above the bottom, where D represents the turbine diameter.

In addition to testing, computational fluid dynamics (CFD) methods are widely employed for predicting the hydrodynamic performance and wake characteristics of HATST Sufian et al. [17] have conducted numerical simulations of HATST under waves and currents utilizing a coupled boundary element method (BEM) and CFD approach, achieving good agreement with experimental data. Schleicher et al. [18] have designed a portable microfluidic power turbine using OpenFOAM. Tian et al. [19] have employed a transient CFD method to evaluate the hydrodynamic performance of HATST under varying wave heights and turbine submersion depths. Similarly, Liu and Park [20] have investigated the impact of waves on HATST by utilizing OpenFOAM, highlighting that the influence of waves on the average power coefficient may be negligible; However, they do affect the flow structure behind the turbine.

Scarlett et al. [21] have made advancements in the conventional boundary element method by integrating dynamic stall and rotationally augmented corrections. This enhanced model incorporates synthesized velocity time series to forecast turbine performance across diverse unsteady conditions. By integrating dynamic stall and rotationally augmented corrections, Scarlett et al. [21] have aimed to improve the accuracy of predictions related to turbine performance under varying flow conditions. In a related study, Qian et al. [22] have conducted a quantitative analysis of the collective impacts of waves, currents, and turbulence intensity on the power generation of a turbine using OpenFAST. Their research highlighted significant effects stemming from wave–current interactions, particularly when waves are oriented in opposition to the current direction. This indicates that the interplay between waves and currents can substantially influence the power generation capabilities of HATST systems. The utilization of OpenFAST allowed for a comprehensive

assessment of these effects, offering insights crucial for optimizing turbine performance in real-world tidal stream environments. Despite the requirement for a significant number of meshes to simulate the actual rotation of the turbine and ensure result accuracy, CFD methods offer insights into the hydrodynamic performance and flow structure of a turbine under wave interaction [23].

In summary, previous research has generally overlooked the influence of wavelength and turbine submergence depth. The exploration of the hydrodynamic performance of horizontal-axis tidal stream turbines (HATST) under wave–flow interaction remains relatively limited. Addressing this gap, this paper utilizes OpenFOAM version 8 to simulate the hydrodynamic performance and flow structure of HATST under waves and currents. The primary focus is on assessing the effects of wave height, wavelength, and turbine submersion depth on turbine performance and flow features behind the turbine. The CFD method presented in this paper can serve as a reference for forthcoming investigations concerning turbines operating within the complex interaction of currents and waves.

2. Methodology

2.1. Governing Equations

In this paper, OlaFlow [24] was utilized for generating waves and currents. OlaFlow [24] is an open-source software built on the OpenFOAM platform, specifically designed for simulating wave dynamics. The program employs finite volume discretization to solve three-dimensional volume-averaged Reynolds-averaged Navier–Stokes equations (VARANS) [25]. It utilizes the volume of fluid (VOF) method to track two incompressible phases (water and air), accurately representing complex free surface variation [20].

The continuity and momentum conservation equations are as follows:

$$\frac{\partial u_i}{\partial x_i} = 0 \tag{1}$$

$$\begin{aligned} &\tfrac{1+C}{\phi}\tfrac{\partial \rho u_i}{\partial t} + \tfrac{1}{\phi}\tfrac{\partial}{\partial x_j}\left[\tfrac{1}{\phi}\rho u_i u_j\right] \\ &\quad = -\tfrac{\partial p^*}{\partial x_i} - g_j X_j \tfrac{\partial \rho}{\partial x_i} + \tfrac{1}{\phi}\tfrac{\partial}{\partial x_j}\left[\mu_e \tfrac{\partial u_i}{\partial x_j}\right] + F_i^{ST} - \alpha \tfrac{(1-\phi)^3}{\phi_3}\tfrac{\mu}{D_{50}^2} u_i \\ &\quad -\beta\left(1 + \tfrac{7.5}{KC}\right)\tfrac{1-\phi}{\phi_3}\tfrac{\rho}{D_{50}}\sqrt{u_i u_j u_j} \end{aligned} \tag{2}$$

where u is the so-called extended averaged or Darcy velocity, ρ is the density, p is the pressure, g is the acceleration of gravity, μ is the dynamic viscosity, ϕ is the porosity, D_{50} is the mean nominal diameter, p^* is the pseudo dynamic pressure, and x is the position vector. α, β, and C are adjustment parameters that need to be chosen based on experimental or theoretical data to represent typical and specific values; KC is the Keulegan–Carpenter number, which introduces additional friction due to the oscillatory nature and unsteadiness of the system. For further details on the governing equations and solution procedures, please refer to Rusche [26] and Higuera et al. [27].

2.2. Wave Theory

When a wave encounters a uniformly distributed current across the water column, the fifth-order Stokes wave theory proves effective in capturing the current modulations of wave dispersion and kinematics [28]. An analytical solution exists for the interaction between a linear wave and a uniform current ($U_{current}$) [29], where the dispersion relation is as follows:

$$(\omega - kU_{current})^2 = gk\tanh kh \tag{3}$$

where ω is the wave frequency, h the water depth, and k the wave number.

At the fifth-order wave theory, the dispersion relation in a uniform current ($U_{current}$) is expressed as follows:

$$(\omega - kU_{current})^2 = gk[C_0 + (0.5Hk)^2 C_2 + (0.5Hk)^4 C_4]^2 \tag{4}$$

where H is the wave height, g is the gravitational acceleration, $C_0 = \sqrt{\tanh kh}$, $C_2 = C_0(2+7S^2)/[4(1-S)^2]$, and $C_4 = C_0(4+32S-116S^2-400S^3-71S^4+146S^5)/[32(1-S)^5]$ with $S = \mathrm{sech}(2kh)$. In the deep water, when $kh \to \infty$, $C_0 = 1$, $C_2 = 1/2$, and $C_4 = 1/8$.

3. Computational Methods

3.1. Three-Dimensional Computational Domain and Boundary Conditions

Figure 1 illustrates the three-dimensional computational domain (x-z plane) and boundary conditions for the case with a submersion depth of 1.5D. The diameter of the 3-bladed turbine model is 0.9 m, as specified in Gaurier et al. [11]. Figure 1 illustrates the typical computational domain, consisting of a cubic domain with dimensions of 2.5λ in length, 5.54D in height, and 3D in width, where λ represents the wavelength, D is the turbine diameter, and H is the wave height. The depicted domain features a middle curve, representing the free surface, with the upper region denoting air and the lower part representing water. Initially, the heights of the air and water are set to 1.1D and 4.44D, respectively [30]. The turbine is positioned at a distance of 1λ from the inlet boundary and submerged at a specified depth beneath the free surface. To facilitate turbine rotation, the arbitrary mesh interface (AMI) method is employed. Wave and tidal current conditions are applied to the inlet boundary, while the hydrodynamic condition is applied to the outlet boundary. Special boundary conditions [24] from OlaFlow are utilized at the inlet and outlet boundaries for wave generation and absorption, respectively. The bottom, side, and top boundaries are set to the free slip condition. Additionally, the volume fraction of the water and air phases are defined as 0 and 1, respectively, and gravity is considered along the z-axis.

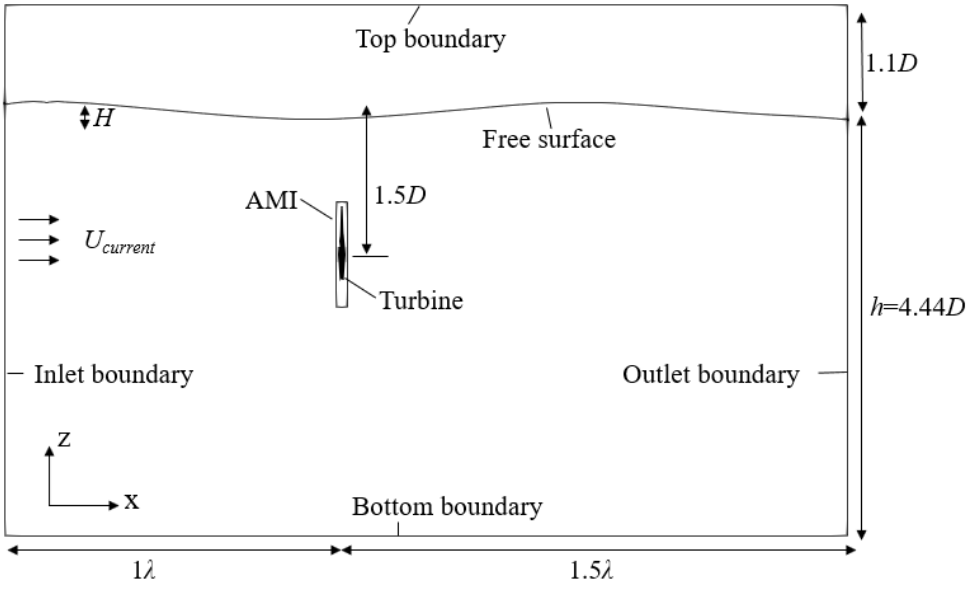

Figure 1. Typical computation domain (x-z plane).

3.2. Numerical Methods

In OpenFOAM, incompressible viscous flow computations are executed through the pressure-based finite volume method (FVM). Pressure is used as the primary variable for determining solution variables. For the time derivative term, a second-order accurate Crank-Nicolson implicit scheme is adopted [18]. Convective terms are discretized using the total variation diminishing (TVD) scheme, while diffusive terms are handled using central differencing. The Reynolds stress terms are closed using the k-ω SST turbulence model [31], and near-wall treatment is applied to the boundary conditions.

3.3. Mesh

The snappyHexMesh tool within OpenFOAM is employed to generate high-quality structured grids for CFD simulations, as depicted in Figure 2 [32]. Grid quality is paramount for result accuracy, particularly in the hydro-performances and wave variations, where mesh resolution around blade surfaces and the free surface significantly influences outcomes. Therefore, mesh refinement is applied around the blades and wave regions. To adequately capture the complexity of waves, a minimum of 80–120 cells per wavelength and 20–40 cells per wave height range are necessary [33]. Adjustments to grid resolution should be made based on varying wave characteristics. This resolution level surpasses the recommended thresholds in the ITTC guidelines [34], which recommends 40 meshes per wavelength and 20 meshes per wave height. However, for other areas, a sparser grid may suffice. In addition to mesh quality, the mesh density also significantly influences the accuracy of CFD results. A finer mesh can improve simulation accuracy, however, this improvement comes with the drawback of longer computation times. Mesh dependency tests are essential for validating the accuracy of simulation results, with particular attention paid to the mesh near the free surface and within the arbitrary mesh interface (AMI) region, as these areas have the most pronounced effect on the outcomes. The authors of [20] have previously carried out the dependency test to obtain the optimal mesh for accurate simulations. The results revealed a significant variance in the power coefficient between the coarse and medium meshes, with a discrepancy of 29.09%. Conversely, the difference observed between the medium and fine meshes was markedly less, at merely 0.69%. Based on these findings, the medium mesh was deemed adequate for the simulations in the current study. It was further determined that the accuracy of the simulation results could be substantially enhanced by employing a fine mesh in critical areas, specifically near the free surface and in the vicinity of the turbine, as illustrated in Figure 2. This strategic placement of the fine mesh is instrumental in capturing the complex flow dynamics around these regions, thereby ensuring the reliability of the simulation outcomes. Additionally, it has been observed that increasing the mesh density within the AMI region has only a limited impact on the results.

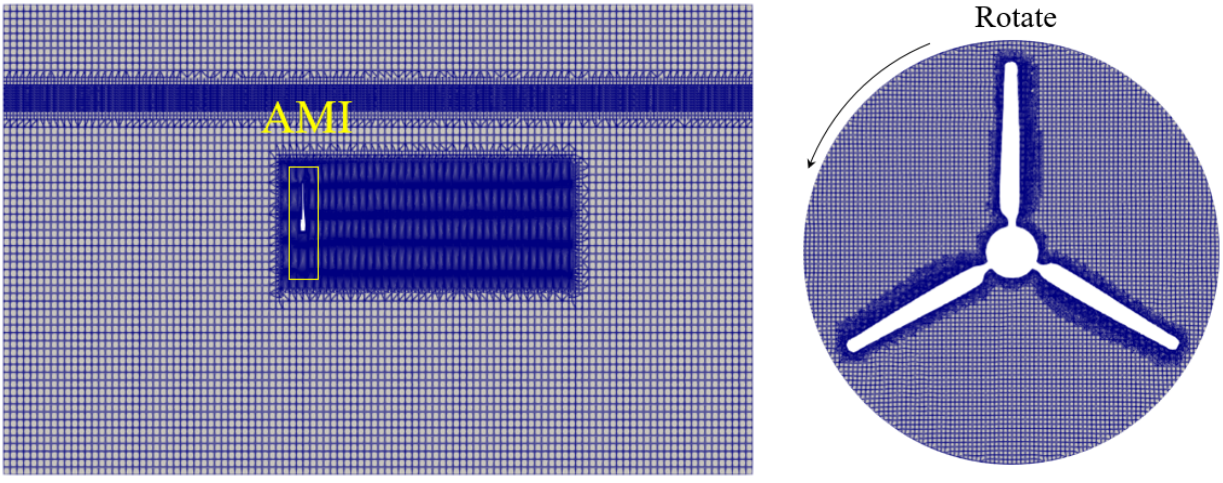

Figure 2. Mesh topology. (**a**) Mesh in the middle plane. (**b**) Mesh in the AMI zone.

3.4. Validation for Waves and Turbine Performance

Typical ocean current turbine sites are often found in channels between islands near the coast, where the environment is sheltered, leading to waves characterized by long periods and relatively small significant wave heights [13]. To simulate these sites, a uniform incoming current flow ($U_{current} = 0.68$ m/s) and a Stokes fifth-order regular wave were

generated from the inlet boundary. The turbine rotated counterclockwise at an angular velocity of 6.7 rad/s, corresponding to tip speed ratio TSR = 4.5. Various wave and depth parameters were considered, as listed in Table 1. Three wavelength and depth ratios (λ/h) were investigated. For the wavelength and depth ratio of 0.8, two wave heights were considered to explore the effect of wave height.

Table 1. Test conditions.

Wavelength and Depth Ratio (λ/h) [-]	Wave Period (T) [s]	Wavelength (λ) [m]	Wave Height (H) [m]
0.8	1.4	3.2	0.1
0.8	1.4	3.2	0.16
1.6	2.0	3.3	0.16
8.7	6.0	34.8	0.16

Figure 3 depicts the simulated wave profiles for various test conditions, showcasing a satisfactory agreement with analytical solutions. To investigate the impact of waves on the submerged depth of the turbine, the vertical velocity component (U_z) was analyzed. Figure 4 illustrates the distribution of U_z with depth for different wave conditions, with comparisons made to results from a numerical model based on boundary element theory [13]. Notably, for identical λ/h ratios, the vertical depth of influence remains consistent. However, when λ/h = 0.2, the wavelength is insufficiently long, resulting in a slight deviation from the theoretical solution despite the overall trend remaining consistent. This suggests a reduction in simulation accuracy, especially for extreme conditions. For depth ratios below 0.2, the wave effects become negligible. Conversely, as the depth ratio becomes excessively large, the vertical velocity component, as predicted by boundary element theory, gradually decreases along the vertical axis while maintaining a certain velocity at the bottom. However, in the vicinity of the actual bottom region, it is imperative for the vertical velocity component to decrease to zero. Consequently, simulation results are deemed more acceptable when they better align with this expectation, reflecting a closer resemblance to physical reality.

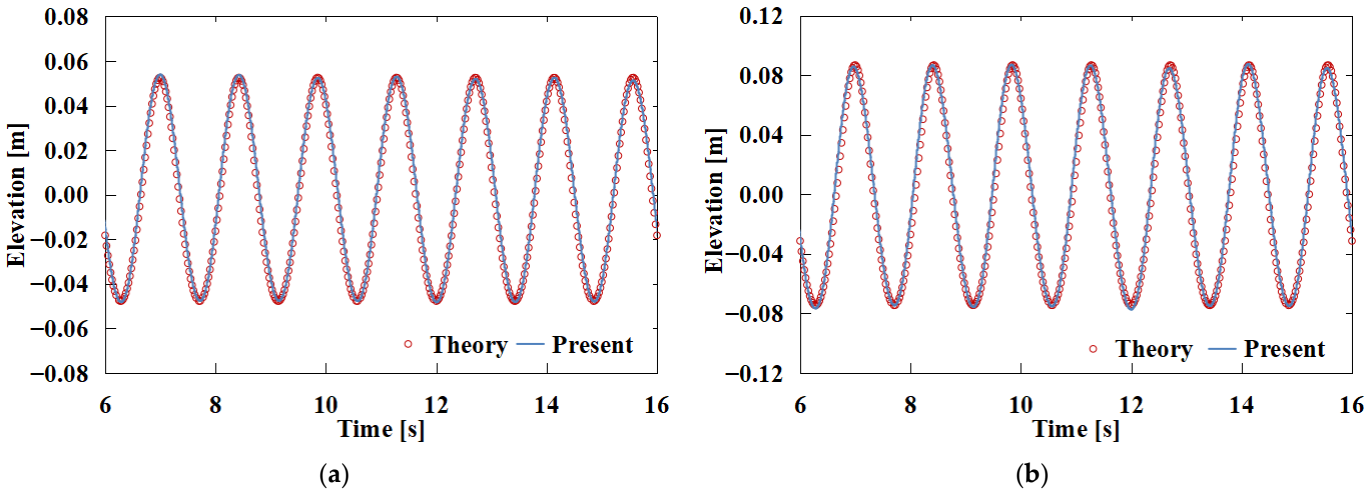

Figure 3. *Cont.*

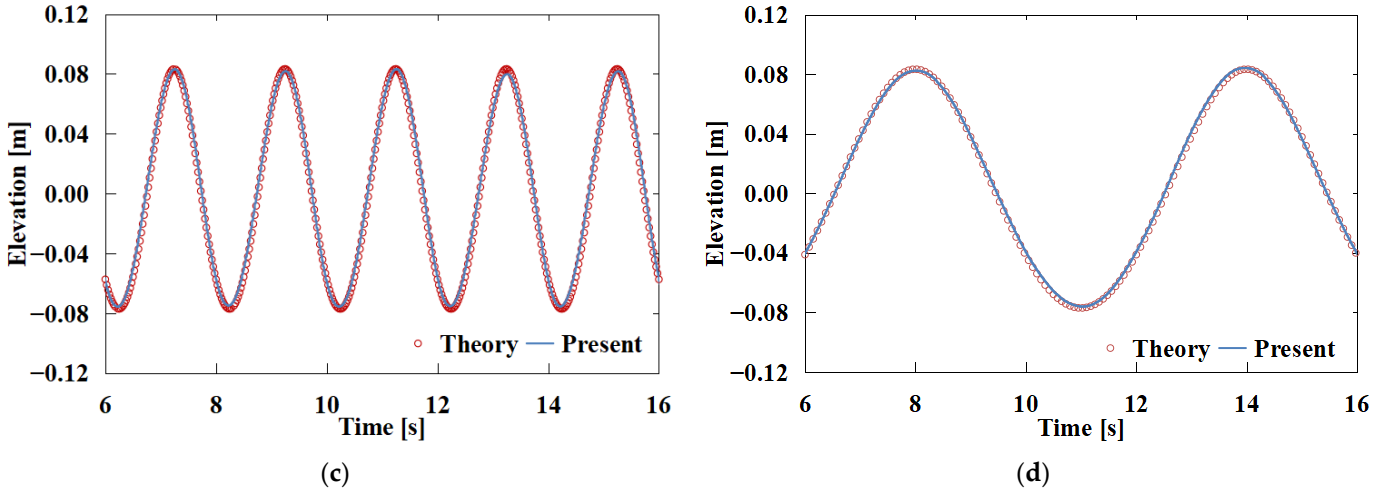

Figure 3. Simulated wave profile for various test conditions. (**a**) $\lambda/h = 0.8$ ($H = 0.1$). (**b**) $\lambda/h = 0.8$ ($H = 0.16$). (**c**) $\lambda/h = 1.6$. (**d**) $\lambda/h = 8.7$.

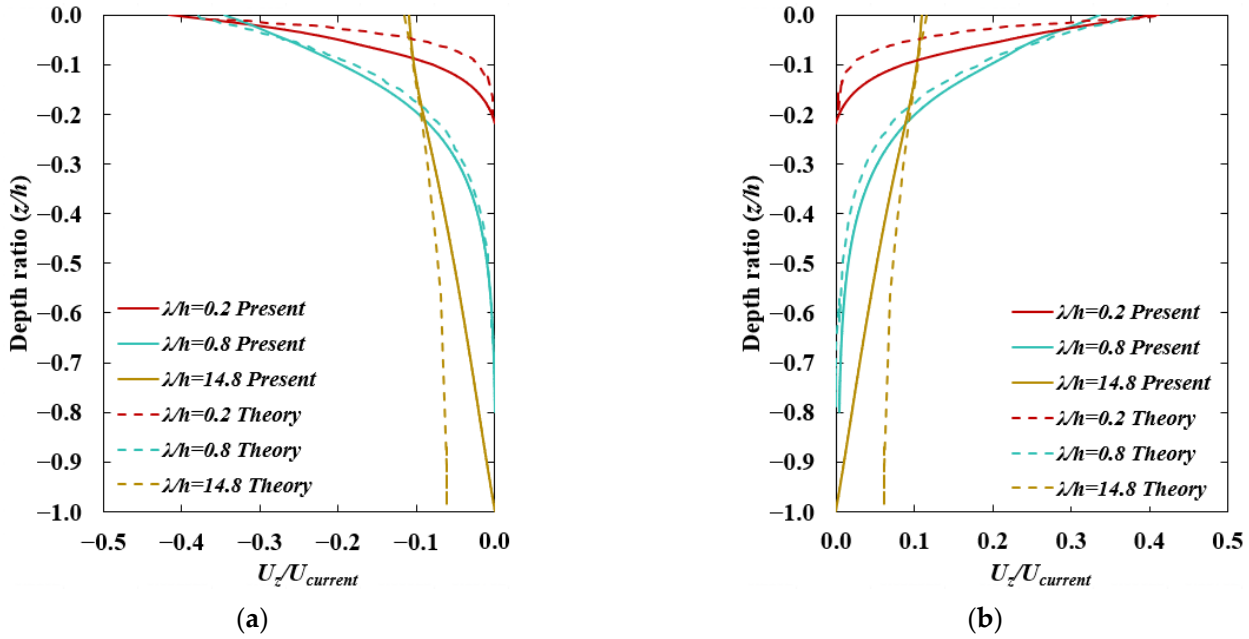

Figure 4. Vertical wave particle velocity (U_z) normalized by the inflow velocity ($U_{current}$) for various λ/h compared with the theory [13]. (**a**) Trough. (**b**) Crest.

The power coefficient (C_p) serves as a crucial parameter denoting the tidal current turbine's capability to convert kinetic energy from the tidal current into mechanical energy. The tip speed ratio (TSR) is defined as the ratio of turbine speed to inflow speed. The power coefficient can be expressed in terms of the pitching moment and the inflow direction load coefficient as follows:

$$C_p = \frac{P}{\frac{1}{2}\rho S U_\infty^3} = \frac{Q\omega}{\frac{1}{2}\rho\pi R^2 U_\infty^3} = \frac{Q}{\frac{1}{2}\rho\pi R^3 U_\infty^2} \times \mathrm{TSR} \tag{5}$$

$$\mathrm{TSR} = \frac{\omega R}{U_\infty} \tag{6}$$

where $S = \pi R^2$ represents the cross-sectional area of the turbine blade and Q denotes the turbine's torque. U_∞ represents the freestream flow and ω is the rotational speed.

Figure 5 presents the power coefficients under waves and currents. The depicted power coefficients exhibit a similar trend to those observed in the experimental data [11]. The wave height was 0.16 m and the corresponding wavelength was 3.2 m, while the submersion depth was equivalent to $1D$. When the TSR was set to 4.5, the turbine's power coefficient reached its maximum, and there was strong agreement between experimental and numerical simulation results. Consequently, TSR = 4.5 was selected for the subsequent cases in the computations.

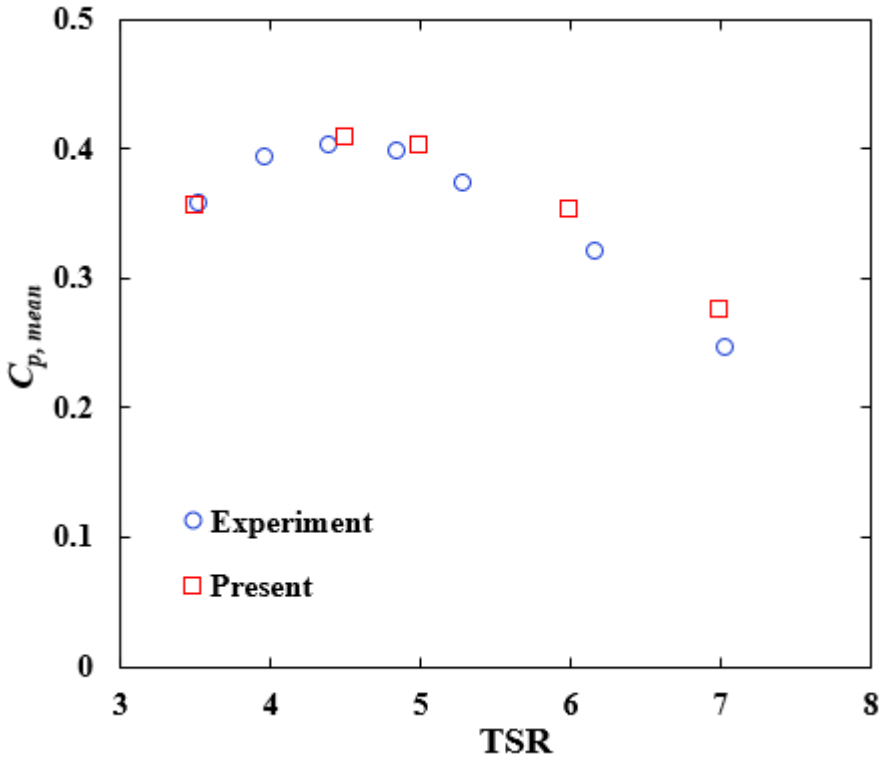

Figure 5. Power coefficients under waves and currents [20].

4. Results and Discussion

The horizontal velocity component (U_x) with depth under the waves was observed. Figure 6 shows the U_x distribution with depth for both the wave crest and trough with turbines positioned at water depths (h) of $1.0D$, $1.5D$, and $2.0D$. Here, D represents the turbine blade diameter. U_x is influenced by both waves and currents, typically attaining maximum and minimum values at the wave crest and trough, respectively. The maximum and minimum U_x values are generally symmetric, with only slight differences near the free surface. The effect of a change in wave elevation is opposite, prompting a focus on the wave crest in this study. The results for various wave heights at $\lambda/h = 0.8$ indicate a notable increase in velocity near the free surface as wave height rises. However, the disparity between maximum and minimum U_x values gradually diminished with increasing submersion depth. When the depth ratio exceeds $2D$, $U_x/U_{current}$ approaches one, indicating minimal wave effects. For waves with longer wavelengths ($\lambda/h = 8.7$), U_x remains nearly constant despite changes in submersion depth, suggesting that longer wavelength waves exert influence at even greater depths.

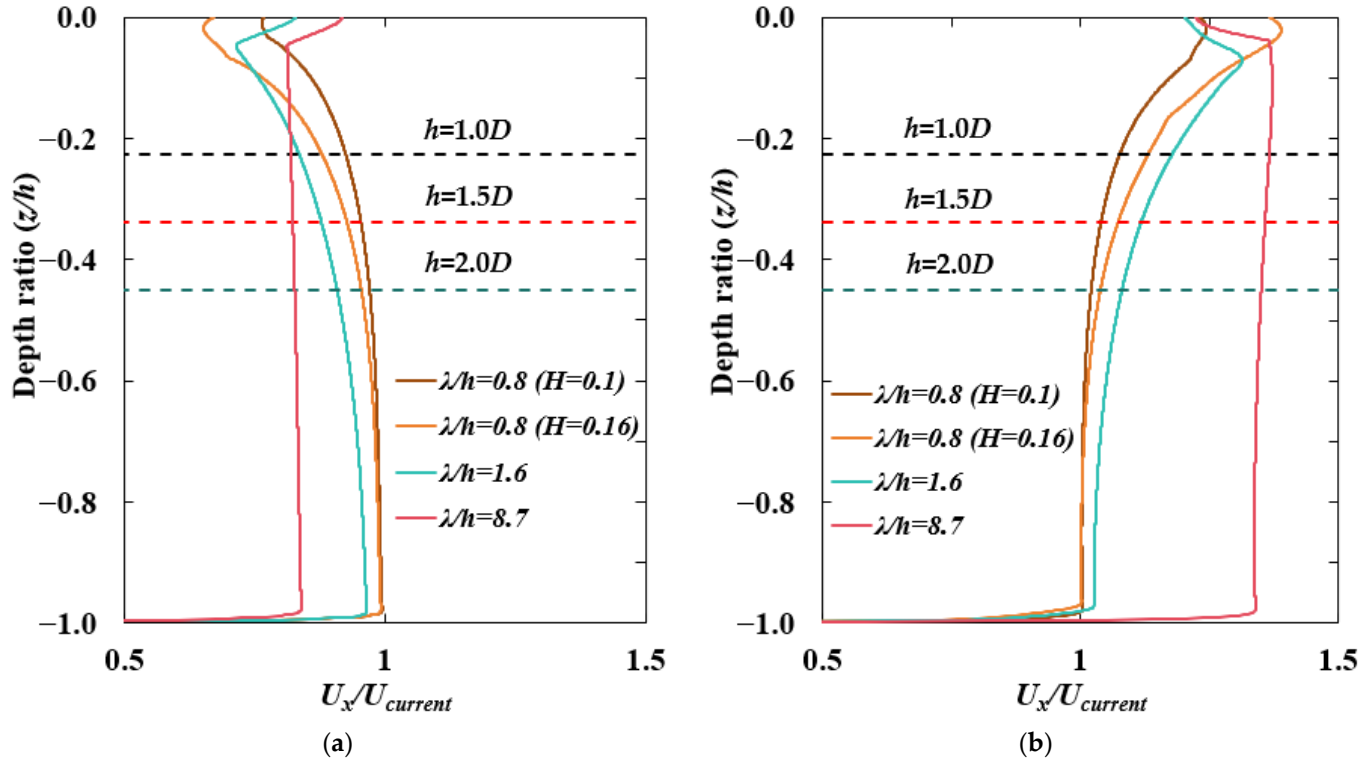

Figure 6. Horizontal wave particle velocity (U_x) normalized by the inflow velocity ($U_{current}$) for various λ/h. (**a**) Trough. (**b**) Crest.

Figure 7 displays the mean power coefficients ($C_{p,mean}$) and standard deviations of power coefficients ($C_{p,std}$) for the turbine under various wave conditions. Notably, the influences of wavelength and wave height on the mean power coefficient appear to be negligible, as indicated by the overlapping error bars. In the experimental setups, the submergence depth of the turbine was set to 1D. It can be observed that the mean power coefficient remained relatively unaffected by the waves [11]. However, as the wavelength increased, there was a tendency for the mean power coefficient to decrease. While wave height and wavelength exhibit minimal impact on the mean power coefficient, their effects on the standard deviation are more pronounced. Specifically, with the exception of longer wavelengths, increasing submersion depth effectively reduces the variation in the power coefficient.

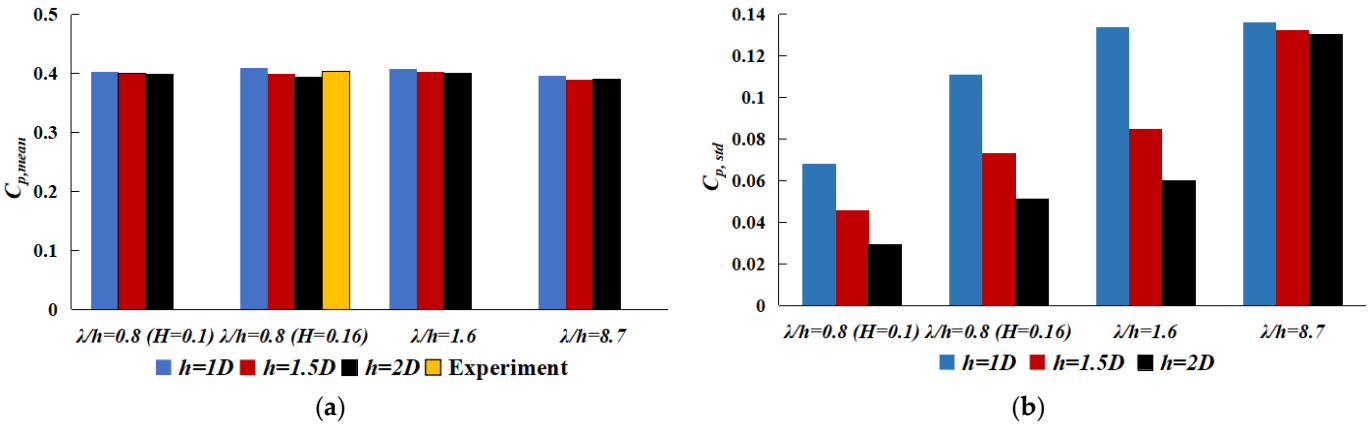

Figure 7. The mean and standard deviation of the turbine power coefficient under different waves. (**a**) $C_{p,mean}$, (**b**) $C_{p,std}$.

Figures 8–11 depict the normalized horizontal velocity contours for various depth ratios. The normalized horizontal velocity is represented as follows [35]:

$$U^* = \frac{U_{current} - U_x}{U_{current}} \times 100\% \quad (7)$$

From the velocity contours, a distinct low-velocity region is observed behind the turbine, where the velocity is lower than the incoming flow. This phenomenon, known as the wake, arises from the interaction of the turbine with the flow. As the wake propagates downstream, there is an exchange of momentum between the low-velocity region and the surrounding high-velocity fluid. Typically, the velocity behind the turbine exhibits a continuous profile along the flow direction, initially decreasing and then gradually increasing. Eventually, the velocity of the wake recovers to match the surrounding velocity [35].

Figures 8 and 9 present the normalized horizontal velocity contours in the xz-plane under $\lambda/h = 0.8$ with H = 0.1 m and H = 0.16 m, respectively, for various depth ratios. For $h = 1.0D$, the center of turbine is positioned at $1.0D = 1.0 \times 0.9$ m $= 0.9$ m. Due to variations in U_x with depth, the wake appears asymmetrical from top to bottom, with larger U^* values observed at the bottom. As the submerged depth increases, U_x behind the turbine experiences rapid growth, while fluctuations become smaller and the wake stabilizes. Notably, the result for H = 0.16 m exhibits a faster increase in U^* behind the turbine compared to the H = 0.1 m result.

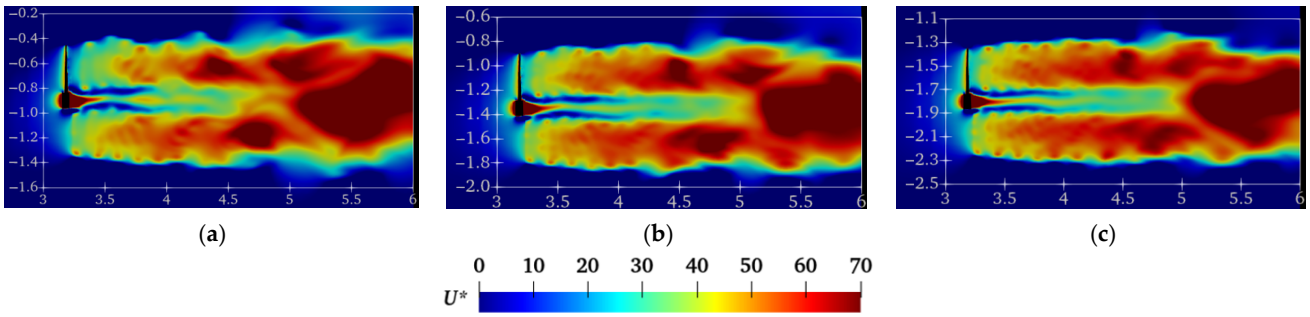

Figure 8. Non-dimensionalized horizontal velocity contours under $\lambda/h = 0.8$ with H = 0.1 m. (**a**) $h = 1.0D$, (**b**) $h = 1.5D$, (**c**) $h = 2.0D$.

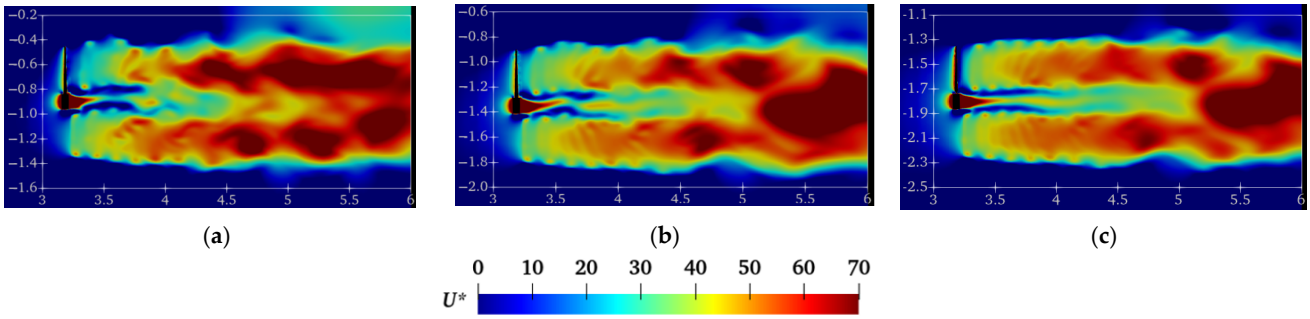

Figure 9. Non-dimensionalized horizontal velocity contours under $\lambda/h = 0.8$ with H = 0.16 m. (**a**) $h = 1.0D$, (**b**) $h = 1.5D$, (**c**) $h = 2.0D$.

Figures 10 and 11 display the normalized horizontal velocity contours in the xz-plane under $\lambda/h = 1.6$ and $\lambda/h = 8.7$ (H = 0.16 m), respectively, for various depth ratios. Under the influence of long wavelength ($\lambda/h = 8.7$), the velocity of the low-velocity region behind the turbine is noticeably higher compared to relatively short wavelength conditions ($\lambda/h = 0.8$ and 1.6). At longer wavelengths, the wake exhibits a more regular pattern compared to shorter wavelengths. With the longer wavelength ($\lambda/h = 8.7$), the overall rise and fall of vortices related to the variation in wave height become more readily apparent and observable.

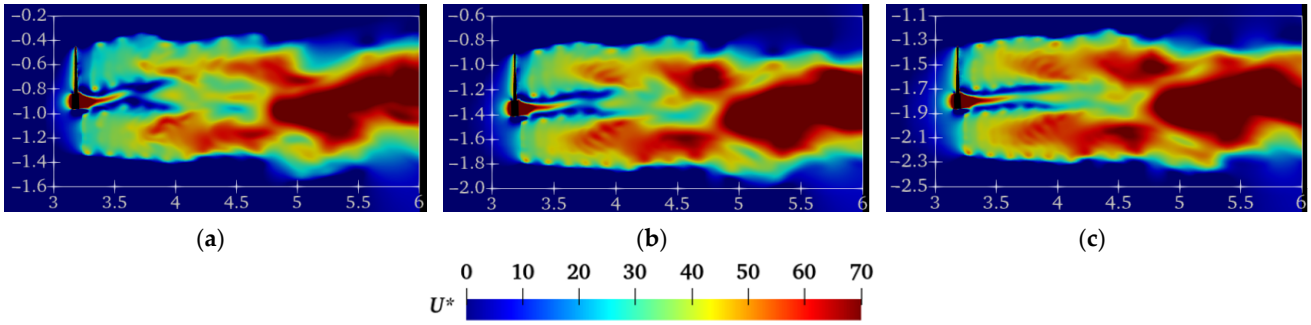

Figure 10. Non-dimensionalized horizontal velocity contours under $\lambda/h = 1.6$. (**a**) $h = 1.0D$, (**b**) $h = 1.5D$, (**c**) $h = 2.0D$.

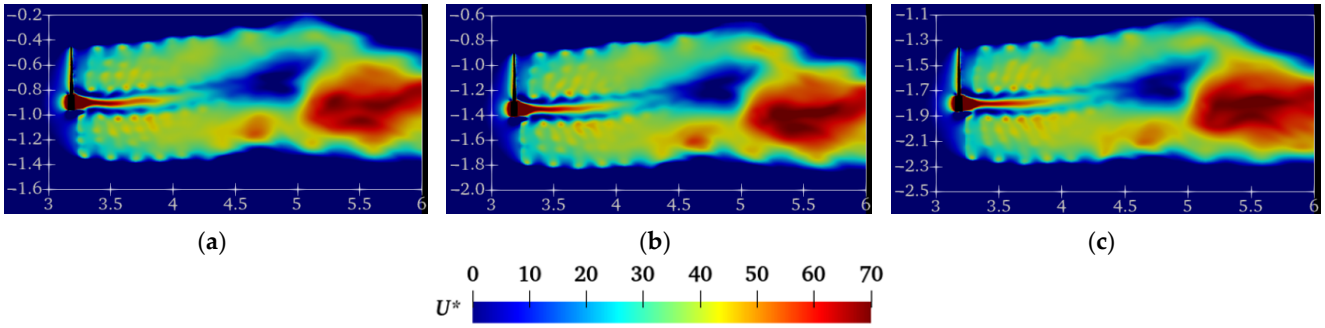

Figure 11. Non-dimensionalized horizontal velocity contours under $\lambda/h = 8.7$. (**a**) $h = 1.0D$, (**b**) $h = 1.5D$, (**c**) $h = 2.0D$.

Figure 12 shows the distribution of vertical velocity (U_z) with depth for the wave crest, with turbines positioned at water depths of $1D$, $1.5D$, and $2D$. The orbital motion of the particles beneath the wave generates the water's vertical velocity (U_z). The depth of the wave crest with turbines positioned at water depths of U_z decreases almost linearly to zero, and U_z near the free surface diminishes as the wavelength increases. Increasing the submersion depth of the turbine effectively mitigates the impact on U_z. However, even at a submersion depth of $2D$, the cases with $\lambda/h = 1.6$ and 8.7 still exhibit significant vertical velocities.

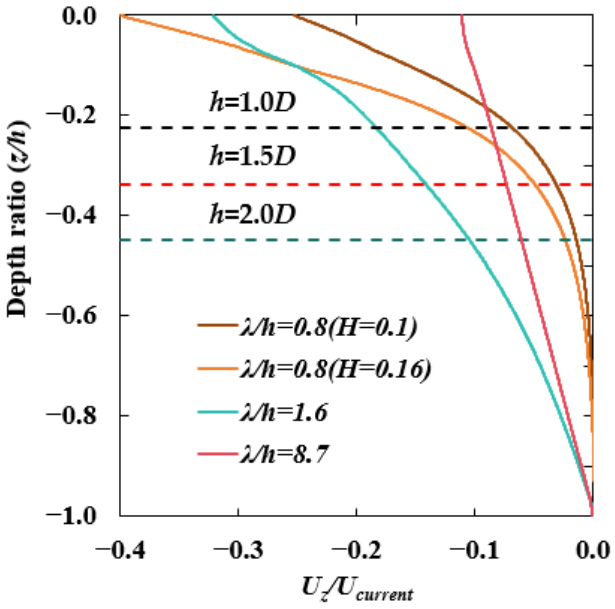

Figure 12. Vertical wave particle velocity (U_z) normalized by the inflow velocity ($U_{current}$) for various λ/h.

Figures 13–16 provide visualizations of the vortex structures behind the turbine under different wave conditions, employing the Q-criterion = 1. The vortical structure around the turbine comprises three main vortices: hub vortices, blade-tip vortices, and thin vortices generated at the trailing edge of the blade. As these vortices evolve, the trailing vortices gradually weaken and dissipate. Upon full development, the blade-tip vortices integrate, amplify, and disperse downstream. The mutual induction pattern between adjacent blade-tip vortices leads to an increase in the horizontal distance of vortices, resulting in a non-uniform velocity distribution in the wake [36].

For the waves with $\lambda/h = 0.8$, the length of the regular vortical structure behind the turbine decreases as the wave height increases. An elevated wave height results in premature disruption of the tip vortices, potentially leading to early vortex breakup and subsequent instability of the wake [35]. A significant low-velocity region is evident around the vortex disruption region. Smaller submersion depths make it easier for the wave to disrupt the wake structure [36]. As the wavelength increases, the velocity variation in the region behind the turbine diminishes, rendering the vortical flow more stable. However, changing the submersion depth has a limited effect on the vortex structure.

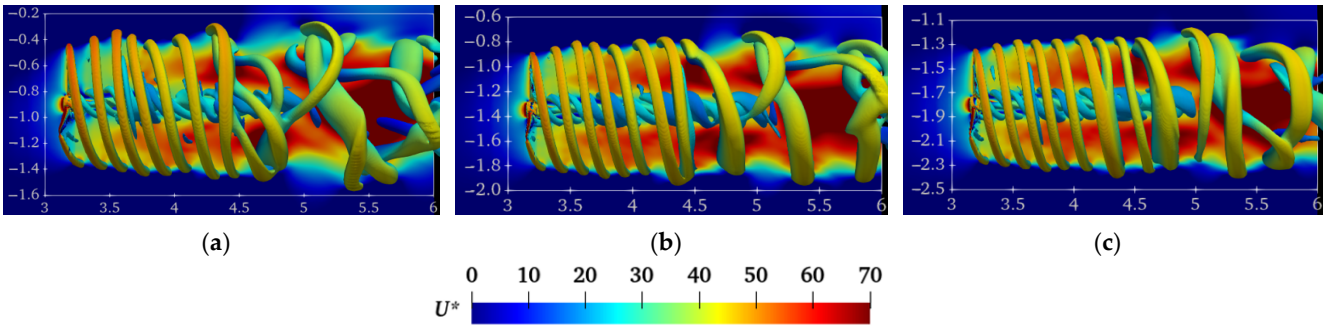

Figure 13. Iso-surface of Q-criterion = 1 under $\lambda/h = 0.8$ and H = 0.1 m. (**a**) $h = 1.0D$, (**b**) $h = 1.5D$, (**c**) $h = 2.0D$.

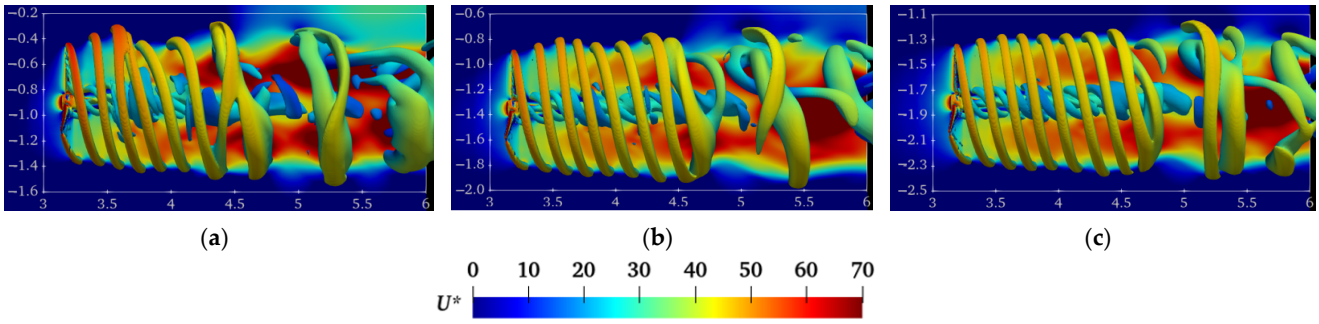

Figure 14. Iso-surface of Q-criterion = 1 under $\lambda/h = 0.8$ and H = 0.16 m. (**a**) $h = 1.0D$, (**b**) $h = 1.5D$, (**c**) $h = 2.0D$.

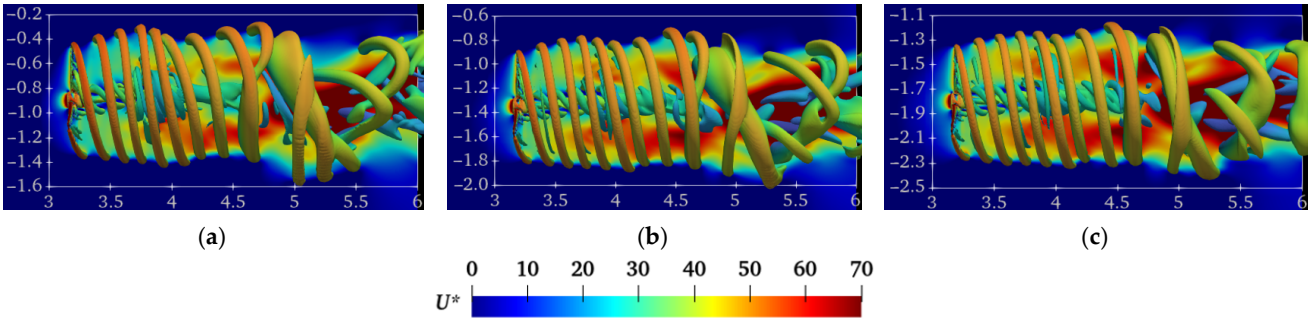

Figure 15. Iso-surface of Q-criterion = 1 under λ/h = 1.6. (**a**) $h = 1.0D$, (**b**) $h = 1.5D$, (**c**) $h = 2.0D$.

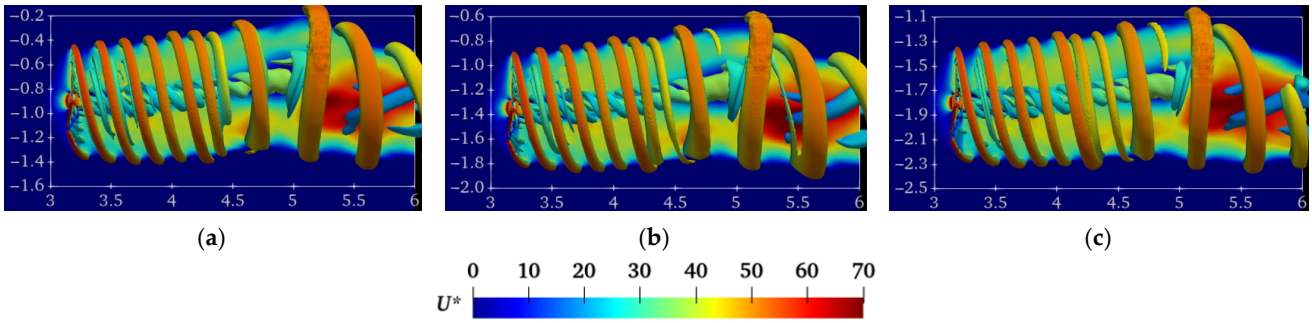

Figure 16. Iso-surface of Q-criterion = 1 under $\lambda/h = 8.7$. (**a**) $h = 1.0D$, (**b**) $h = 1.5D$, (**c**) $h = 2.0D$.

In contrast to the case with only current, when waves and current interact, the motion of a water particle is influenced by the motion of the free surface. Consequently, the change in U_z becomes more complex. Figure 17 shows the vortical flow behind the turbine and U_z contours under $\lambda/h = 0.8$ with H = 0.16 m when the submersion depth is $1D$. In this case, the radius of the vortical flow fluctuates due to variations in U_z. The influence of waves leads to variations in U_z, causing fluctuations in the flow direction of vorticity as a result.

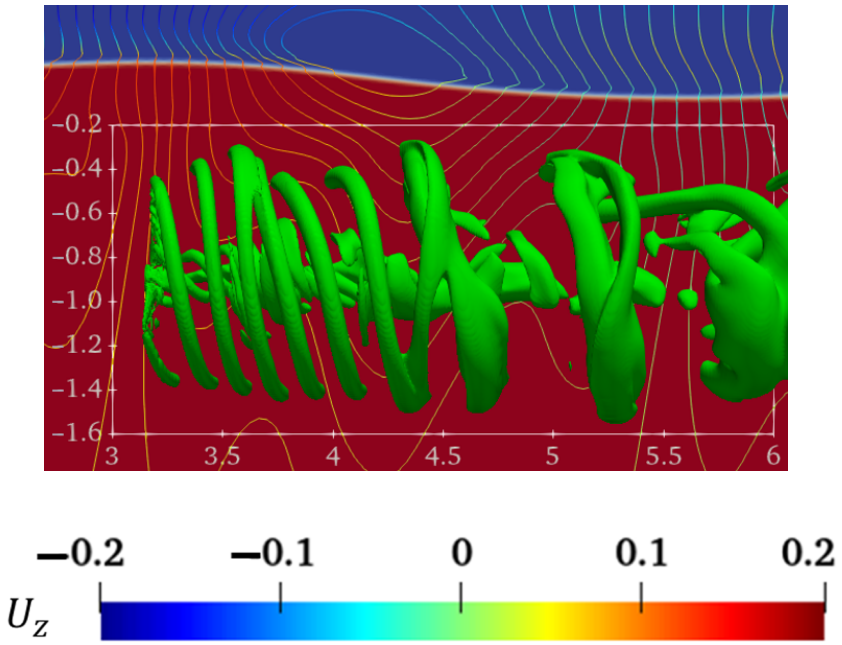

Figure 17. Vortical flow and U_z contours under $\lambda/h = 0.8$ with H = 0.16 (Blue color in the background is air phase, while red color is water phase).

5. Concluding Remarks

This paper investigates the effects of different wave conditions and submersion depths on the performance and fluid flow of a current turbine. The simulations are conducted using the OpenFOAM platform, while OlaFlow is utilized to generate waves and currents. To validate the accuracy of the selected methodology, simulation results are compared with experimental and analytical solutions.

While the impact of waves on the mean power performance of turbines may be negligible, they introduce fluctuations in power output. As wave height and wavelength increase, these fluctuations are amplified, potentially affecting generator maintenance and turbine system fatigue. Increasing the submersion depth can mitigate the influence of waves to some extent, although its effectiveness diminishes for longer waves.

Increasing wave height or reducing wavelength indeed complicates the vortical flow behind the turbine and diminishes the length of regular vortical structures. Vortex struc-

tures exhibit varying radii, which fluctuate based on the distribution of vertical velocity. These interactions offer valuable insights into understanding how waves impact turbine performance. The findings from this present study can offer practical insights for improving the design, installation, and evaluation of the environmental impact of turbines.

Author Contributions: Conceptualization, B.L. and S.P.; methodology, B.L. and S.P.; validation B.L. and S.P.; simulation, B.L.; formal analysis, B.L.; writing—original draft preparation, B.L.; writing—review and editing, B.L. and S.P.; visualization, B.L.; supervision S.P.; funding acquisition, S.P. All authors have read and agreed to the published version of the manuscript.

Funding: This research was supported by the National Research Foundation of Korea (NRF-2021R1I1A3044639).

Institutional Review Board Statement: Not Applicable.

Informed Consent Statement: Not Applicable.

Data Availability Statement: Data are contained within the article.

Conflicts of Interest: The authors declare no conflicts of interest.

References

1. King, J.; Tryfonas, T. Tidal stream power technology–state of the art. In Proceedings of the OCEANS 2009-EUROPE, Bremen, Germany, 11–14 May 2009; pp. 1–8.
2. Afgan, I.; McNaughton, J.; Rolfo, S.; Apsley, D.D.; Stallard, T.; Stansby, P. Turbulent flow and loading on a tidal stream turbine by LES and RANS. *Int. J. Heat Fluid Flow* **2013**, *43*, 96–108. [CrossRef]
3. Tian, W.; VanZwieten, J.H.; Pyakurel, P.; Li, Y. Influences of yaw angle and turbulence intensity on the performance of a 20 kW in-stream hydrokinetic turbine. *Energy* **2016**, *111*, 104–116. [CrossRef]
4. Marsh, P.; Ranmuthugala, D.; Penesis, I.; Thomas, G. Three-dimensional numerical simulations of straight-bladed vertical axis tidal turbines investigating power output, torque ripple and mounting forces. *Renew. Energy* **2015**, *83*, 67–77. [CrossRef]
5. Tian, W.; Mao, Z.; Ding, H. Design, test and numerical simulation of a low-speed horizontal axis hydrokinetic turbine. *Int. J. Nav. Archit. Ocean Eng.* **2018**, *10*, 782–793. [CrossRef]
6. Ng, K.-W.; Lam, W.-H.; Ng, K.-C. 2002–2012: 10 Years of Research Progress in Horizontal-Axis Marine Current Turbines. *Energies* **2013**, *6*, 1497–1526. [CrossRef]
7. Morandi, B.; Di Felice, F.; Costanzo, M.; Romano, G.P.; Dhomé, D.; Allo, J.C. Experimental investigation of the near wake of a horizontal axis tidal current turbine. *Int. J. Mar. Energy* **2016**, *14*, 229–247. [CrossRef]
8. Wang, S.-Q.; Li, C.-Y.; Zhang, Y.; Jing, F.-M.; Chen, L.-F. Influence of pitching motion on the hydrodynamic performance of a horizontal axis tidal turbine considering the surface wave. *Renew. Energy* **2022**, *189*, 1020–1032. [CrossRef]
9. Ahmadi, M.H.B. Influence of upstream turbulence on the wake characteristics of a tidal stream turbine. *Renew. Energy* **2019**, *132*, 989–997. [CrossRef]
10. Lust, E.E.; Luznik, L.; Flack, K.A.; Walker, J.M.; Van Benthem, M.C. The influence of surface gravity waves on marine current turbine performance. *Int. J. Mar. Energy* **2013**, *3–4*, 27–40. [CrossRef]
11. Gaurier, B.; Davies, P.; Deuff, A.; Germain, G. Flume tank characterization of marine current turbine blade behaviour under current and wave loading. *Renew. Energy* **2013**, *59*, 1–12. [CrossRef]
12. Galloway, P.W.; Myers, L.E.; Bahaj, A.S. Quantifying wave and yaw effects on a scale tidal stream turbine. *Renew. Energy* **2014**, *63*, 297–307. [CrossRef]
13. Guo, X.; Yang, J.; Gao, Z.; Moan, T.; Lu, H. The surface wave effects on the performance and the loading of a tidal turbine. *Ocean Eng.* **2018**, *156*, 120–134. [CrossRef]
14. Draycott, S.; Payne, G.; Steynor, J.; Nambiar, A.; Sellar, B.; Venugopal, V. An experimental investigation into non-linear wave loading on horizontal axis tidal turbines. *J. Fluids Struct.* **2019**, *84*, 199–217. [CrossRef]
15. Zang, W.; Zheng, Y.; Zhang, Y.; Zhang, J.; Fernandez-Rodriguez, E. Experiments on the mean and integral characteristics of tidal turbine wake in the linear waves propagating with the current. *Ocean Eng.* **2019**, *173*, 1–11. [CrossRef]
16. Kolekar, N.; Banerjee, A. Performance characterization and placement of a marine hydrokinetic turbine in a tidal channel under boundary proximity and blockage effects. *Appl. Energy* **2015**, *148*, 121–133. [CrossRef]
17. Sufian, S.F.; Li, M.; O'Connor, B.A. 3D modelling of impacts from waves on tidal turbine wake characteristics and energy output. *Renew. Energy* **2017**, *114*, 308–322. [CrossRef]
18. Schleicher, W.C.; Riglin, J.D.; Oztekin, A. Numerical characterization of a preliminary portable micro-hydrokinetic turbine rotor design. *Renew. Energy* **2015**, *76*, 234–241. [CrossRef]
19. Tian, W.; Ni, X.; Mao, Z.; Zhang, T. Influence of surface waves on the hydrodynamic performance of a horizontal axis ocean current turbine. *Renew. Energy* **2020**, *158*, 37–48. [CrossRef]

20. Liu, B.; Park, S. CFD Simulations of the Effects of Wave and Current on Power Performance of a Horizontal Axis Tidal Stream Turbine. *J. Mar. Sci. Eng.* **2023**, *11*, 425. [CrossRef]
21. Scarlett, G.T.; Sellar, B.; van den Bremer, T.; Viola, I.M. Unsteady hydrodynamics of a full-scale tidal turbine operating in large wave conditions. *Renew. Energy* **2019**, *143*, 199–213. [CrossRef]
22. Li, Q.; Venugopal, V.; Barltrop, N. Modelling dynamic loadings of a tidal stream turbine in combined wave-current-turbulence environment. *Sustain. Energy Technol. Assess.* **2022**, *50*, 101795. [CrossRef]
23. Holst, M.A.; Dahlhaug, O.G.; Faudot, C. CFD Analysis of Wave-Induced Loads on Tidal Turbine Blades. *IEEE J. Ocean. Eng.* **2015**, *40*, 506–521. [CrossRef]
24. Higuera, P. Enhancing active wave absorption in RANS models. *Appl. Ocean Res.* **2020**, *94*, 102000. [CrossRef]
25. del Jesus, M.; Lara, J.L.; Losada, I.J. Three-dimensional interaction of waves and porous coastal structures. *Coast. Eng.* **2012**, *64*, 57–72. [CrossRef]
26. Rusche, H. Computational Fluid Dynamics of Dispersed Two-Phase Flows at High Phase Fractions. Ph.D. Thesis, Imperial College London, University of London, London, UK, 2003.
27. Higuera, P.; Lara, J.L.; Losada, I.J. Realistic wave generation and active wave absorption for Navier–Stokes models. *Coast. Eng.* **2013**, *71*, 102–118. [CrossRef]
28. Fenton John, D. A Fifth-Order Stokes Theory for Steady Waves. *J. Waterw. Port Coast. Ocean Eng.* **1985**, *111*, 216–234. [CrossRef]
29. Dean, R.G.; Dalrymple, R.A. *Water Wave Mechanics for Engineers and Scientists*; World Scientific Publishing Company: Singapore, 1991; Volume 2.
30. Ng'aru, J.M.; Park, S. Computational Analysis of Cavitating Flows around a Marine Propeller Using Incompressible, Isothermal Compressible, and Fully Compressible Flow Solvers. *J. Mar. Sci. Eng.* **2023**, *11*, 2199. [CrossRef]
31. Menter, F.R. Two-equation eddy-viscosity turbulence models for engineering applications. *AIAA J.* **1994**, *32*, 1598–1605. [CrossRef]
32. Ng'aru, J.M.; Park, S. CFD Simulations of the Effect of Equalizing Duct Configurations on Cavitating Flow around a Propeller. *J. Mar. Sci. Eng.* **2022**, *10*, 1865. [CrossRef]
33. Jeon, W.; Park, S.; Cho, S. Moored motion prediction of a semi-submersible offshore platform in waves using an OpenFOAM and MoorDyn coupled solver. *Int. J. Nav. Archit. Ocean Eng.* **2023**, *15*, 100544. [CrossRef]
34. ITTC. Recommended Procedures and Guidelines; Resistance Test; 2011. Available online: https://ittc.info/media/1403/index.pdf (accessed on 24 March 2024).
35. Zhang, Y.; Wei, W.; Zheng, J.; Peng, B.; Qian, Y.; Li, C.; Zheng, Y.; Fernandez-Rodriguez, E.; Yu, A. Quantifying the surge-induced response of a floating tidal stream turbine under wave-current flows. *Energy* **2023**, *283*, 129072. [CrossRef]
36. Chen, G.; Liang, X.-F.; Li, X.-B. Modelling of wake dynamics and instabilities of a floating horizontal-axis wind turbine under surge motion. *Energy* **2022**, *239*, 122110. [CrossRef]

Disclaimer/Publisher's Note: The statements, opinions and data contained in all publications are solely those of the individual author(s) and contributor(s) and not of MDPI and/or the editor(s). MDPI and/or the editor(s) disclaim responsibility for any injury to people or property resulting from any ideas, methods, instructions or products referred to in the content.